

# DeepSolarEye: Power Loss Prediction and Weakly Supervised Soiling Localization via Fully Convolutional Networks for Solar Panels

Sachin Mehta<sup>\*†</sup>, Amar P. Azad<sup>†</sup>, Saneem A. Chemmengath<sup>†</sup>, Vikas Raykar<sup>†</sup>, and Shivkumar Kalyanraman<sup>†</sup>

<sup>\*</sup>University of Washington, Seattle, USA

<sup>†</sup>IBM Research Lab, India

Email: sacmehta@uw.edu, {amarazad, saneem.cg, viraykar, shivkumar-k}@in.ibm.com

**Abstract**—Impact of soiling on solar panels is an important and well-studied problem in renewable energy sector. In this paper, we present a novel approach based on fully convolutional networks which takes an RGB image of solar panel and environmental factors (optional) as inputs to predict power loss, soiling localization, and soiling type. In computer vision, predicting localization is a complex task which typically requires human labeled data such as bounding boxes or segmentation masks. Our proposed approach consists of specialized four stages which completely avoids human labeled localization data and only needs panel images with power loss for training. The region of impact area obtained from the localization masks are then classified into soiling types using the *webly supervised* learning. For superior localization capabilities of convolutional neural networks (CNNs), we introduce a novel bi-directional input-aware fusion (BiDIAF) block that reinforces the input at different levels of CNN to learn input-specific feature maps. Our empirical study shows that BiDIAF improves the power loss prediction accuracy and the localization Jaccard index of ResNet by about 3% and 4% respectively. Our end-to-end model yields further improvement of about 24% on localization task when learned in a weakly supervised manner. Our approach is generalizable and showed promising results on web crawled solar panel images. Additionally, we collected first of its kind dataset for solar panel image analysis consisting 45,000+ images.

## I. INTRODUCTION

The surge in solar photovoltaic (PV) based renewable energy in recent years has revolutionized the energy sector across the globe by greatly reducing the energy cost [1]. Growing number of large- and mid-sized solar farms often face operations and maintenance challenges. Various environment induced soiling on solar panel (accumulation of dust, pollen, leaves, bird drop, snail trail, and snow) and defects, such as cracks, hamper the power generation at large [2]–[5]. Automatic visual inspection-based solutions can play a vital role in efficient solar farm operations, maintenance, and asset warranty.

The type of soiling or defect on the panel can be instantly and effortlessly recognized by merely looking at the PV panel image. However, to analyze the impact of soiling or defect on the performance of the solar panel, we need to know more details such as soiling amount and coverage, type of the material, and location on the panel. Such a detailed information is not only helpful for estimating the impact on the performance of solar panel, but also helpful for recommending corrective measures; which together are critical for efficient solar farm maintenance. As an example, *wiping* is a more appropriate cleaning action when solar panel is covered with a bird drop rather than air blow which is useful for cleaning dust (see Figure 1(d) and (c)). This decision is likely due to

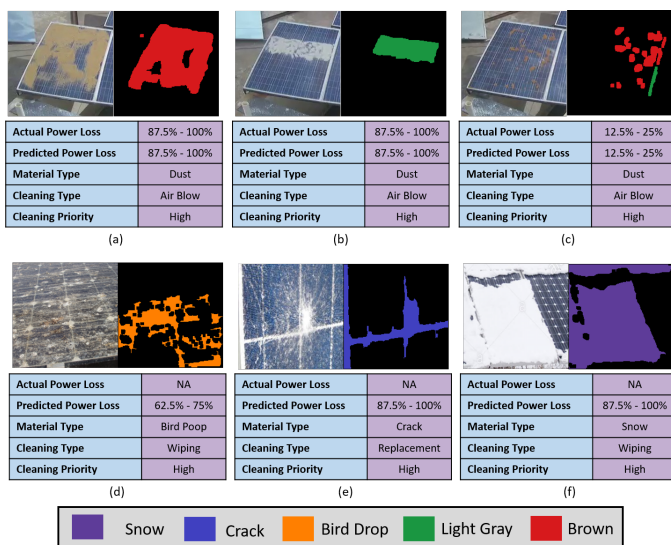


Fig. 1: Six images depicting the performance of our method. First three images are from our dataset while the remaining three are downloaded from the Internet. Our method can efficiently localize PV soiling and type, even in the wild. See Appendix C for more images. Best viewed in color.

the nature of the material, e.g., bird drop has sticky and oily composition than dust.

Besides soiling coverage and type, soiling location also plays a vital role in impact prediction due to the physics of cell connections in panel. As an example, dust cover on panels in Figure 1(b) is very less compared to that in Figure 1(a), however, power loss is similarly high in both the cases. This can be explained by cell connection physics of the panel. By design, solar panels have cells in series in vertical columns and one bypass diode per two columns. Therefore, even if one cell is fully covered by dust, it can block the current for the entire bypass diode segment; thus resulting in high power loss.

The aim of this paper is to develop a model to simultaneously predict power loss, soiling localization, and soiling category given a solar panel image. Deep convolutional neural networks (CNNs) have performed well in visual recognition tasks such as image classification, object detection, and segmentation. Yet, application of CNNs in solar farm monitoring still remains a challenge; primarily due to lack of labeled dataset. In this paper, we present a novel end-to-end fully convolutional neural network, *DeepSolarEye*, that simultaneously predicts the power loss and localizes soiling area from the RGB

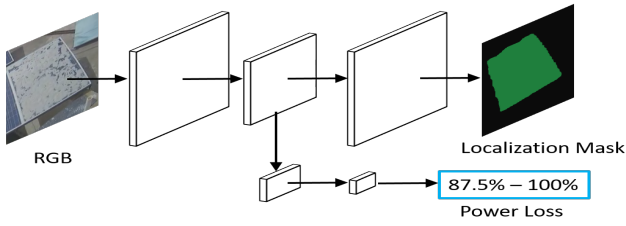


Fig. 2: Overview of our method, DeepSolarEye, that predicts impact on the power loss and the soiling area simultaneously.

image of solar panel. A simplified overview of DeepSolarEye is presented in Figure 2. Ideally, to train such a model, we need two kinds of labels: 1) power loss, and 2) localization mask. In our approach, DeepSolarEye, we bypass the explicitly labeled localization data requirement by using power loss label as weak supervision for localization. This is in contrast to most of the existing segmentation and localization methods (e.g. [6], [7]), which requires labeled localization data.

To the best of our knowledge, we are the first to propose a deep learning approach for solar panel soiling and defect analysis. The key contributions of our work are:

- **Weakly supervised learning:** The proposed *DeepSolarEye* consists of four step approach as follows: 1) train a CNN-based classification network, *ImpactNet*, for predicting the power loss due to soiling or defect, 2) create a candidate soiling mask using a pyramid-based approach from the classification network, 3) train a multi-task network, *Mask FCNN*, for simultaneously predicting the power loss and localizing the soiling area using the generated candidate mask, and 4) predict the soiling category using weakly supervised neural network, *WebNN*.
- **BiDIAF unit for accurate localization:** CNN learn features at multiple spatial levels by performing convolution and down-sampling operations. However, feature maps learned by CNNs does not encode localization information explicitly; thereby hindering in localizing the impact area. Localization further becomes difficult due to down-sampling operations as spatial information is lost due to these operations. To overcome these challenges, we introduce a novel convolutional unit, a bi-directional input-aware fusion (BiDIAF), that reinforces the input at different level of CNNs to learn input-specific feature maps. We show that BiDIAF units improve the localization capabilities of CNNs largely.
- **Dataset:** We created first of its kind dataset for solar panel image analysis, comprising of 45,754 solar panel images with corresponding power loss, solar irradiance, and timestamp.

Our experimental results suggest that our end-to-end system achieves good localization and classification results. In particular, our end-to-end system which is trained with noisy candidate localization masks improves the localization accuracy by 24%. Further, our approach leverages weakly supervised method for determining the type of soiling such as dust,

bird drop, and crack; therefore enables extensibility for future soiling type that are not present in the dataset without re-training the CNN model. For example, crack and snow were detected and classified despite being not present in our dataset (see Figure 1(d) and (e)).

## II. RELATED WORK

### A. Image-based solutions for solar panel analysis

There exist some work for analyzing different soiling types [8]–[11]. These methods take RGB or IR<sup>1</sup> image as an input and applies a traditional image processing algorithm, such as histogram matching, filtering, and color-space conversion. The output of the image processing algorithm is then thresholded to locate the impact area. As these methods are threshold bound, they are not scalable to identify different types of soiling. Further, these methods are not able to capture the complex relations between different factors, such as particle size, thickness, and coverage along with environmental factors (e.g. solar irradiance and humidity), that are required for analyzing the impact on power loss.

### B. CNN for visual recognition tasks

Convolutional Neural Networks (CNNs) are the state-of-the-art methods for image classification [12]–[15]. Recent classification architectures have explored different types of connectivity patterns, such as bypass connections in [14] and dense connections in [15], to improve the information flow inside the network; thereby enabling end-to-end training of very deep CNNs. Further, these classification networks have been used as the base feature extractors for several visual recognition tasks including object detection [6] and segmentation [16], indicating features aggregated by these networks are robust.

Region-based CNNs or R-CNNs [17] have proven to be effective for both detection and segmentation tasks. However, the accuracy of R-CNNs is dependent on the region proposal method. Unlike R-CNNs, fully convolutional networks (FCN) have gained attention as they enable end-to-end training and are fast (e.g. [6], [18]). The features learned by the classification network at lower spatial resolution (say  $7 \times 7$ ) are coarse and leads to coarse output (e.g. segmentation masks of FCN-32s [19]). To address this limitation, several techniques have been proposed such as fully convolutional region proposal networks (e.g. [6]), skip-connections (e.g. [19], [20]), deconvolutional networks (e.g. [18]), and multiple-input networks (e.g. [21]).

Several FCN-based supervised object classification and localization networks exists in literature. Yet, extending these approaches to new domains still remains challenging; primarily due to the non-availability of large labeled datasets that are required for training CNNs. In this paper, we propose a method for PV Solar image analysis that addresses this. Our method consists of novel and carefully designed components that allows extending the previous work on image classification and localization on a new dataset *without* any human labeled localization data.

<sup>1</sup>IR-based systems exploit the overheating phenomenon while RGB-based systems exploit the color information to locate the hot-spots.

### III. DATASET

We create first of its kind dataset, *PV-Net*, comprising of 45,754 images of solar panels with power loss. Our experimental setup consists of two identical solar panels, which are kept side by side with an RGB camera facing them. Soiling experiments were conducted on the first panel (close to the camera) while the other panel was used for reference purpose. Images were captured at every 5 seconds and corresponding power generated by the panels were recorded (see Figure 3). Soiling impact is reported as the *percentage power loss* with respect to the reference panel. We will be using soiling impact and power loss interchangeably in this paper.

Our data recording methodology was aimed to capture various types of soiling and its impact on PV panel. For this, we exposed the panel with different types of soiling in terms of color (red, brown, and gray), particle size (sand, dust, and talcum powder), and thickness under natural environmental conditions [2]. Some of the thick patches corresponds to high power loss as much as 90%. The data set was collected for about a month and was enriched with large variations in soiling due to both experimental (e.g. dust with varying thickness, blob sizes, and patches) and natural means (e.g. wind and precipitation). Besides power loss corresponding to the soiled panel, our data set also contains information about environmental factors (solar irradiance and timestamp information).

### IV. DEEPSOLAREYE

We propose an end-to-end system, DeepSolarEye, which is based on fully convolutional networks. The architecture of DeepSolarEye is visualized in Figure 4. The input to our system is an RGB image with an optional environmental factors (such as solar irradiance and time-stamp), while outputs of our system are: (1) soiling impact, (2) soiling localization, and (3) soiling category. We propose a four step approach that enables the training of DeepSolarEye with automatic data labeling, as follows: 1) train a CNN-based classification network, *ImpactNet*, for predicting soiling impact, 2) create the candidate mask by aggregating the feature maps learned by classification network at different spatial-levels using pyramid-based approach, 3) train a multi-task network, *Mask FCNN*, for simultaneously predicting the soiling impact and soiling localization mask, and 4) predict the category of soiling using

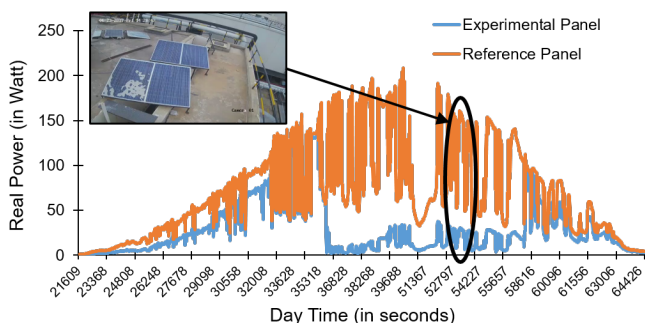


Fig. 3: Graph showing the power generated by reference and experimental panel through out the day.

webly supervised neural network, *WebNN*. These steps are discussed in detail below.

#### A. ImpactNet: Image to Impact Analysis

Traditional CNNs encode the spatial information about the objects present in an image by performing convolution and down-sampling operations in a top-down fashion. Though these CNNs does not encode the localization information, one may combine the feature maps at multiple spatial levels using a bottom-up approach to localize the object. However, the down-sampling operations involved in CNNs tend to loose the spatial information and may hinder in object localization. To address this limitation, we introduce a novel “bi-directional input-aware fusion block (BiDIAF)” that reinforces the input inside the network to compensate the loss of spatial information; thereby helping the network to learn the features that are relevant with respect to the input. BiDIAF block takes an input from the main CNN branch ( $\mathbf{x}_M$ ) and shares one of the output with same branch, hence we call this unit as *bi-directional* input-aware fusion unit.

Our proposed unit can be integrated with any CNN (such as VGG [12] or ResNet [14]). Following the success of ResNet [14] in different visual recognition tasks, we choose ResNet as our baseline network. ResNet stacks residual convolutional units (RCU) to aggregate feature maps at different spatial levels. The input and output in RCU is connected through an identity mapping, which improves the information flow inside the network and prevents vanishing gradient issue. We add the BiDIAF unit between two residual convolutional units (RCU), as shown in Figure 4. BiDIAF takes the output of previous RCU  $\mathbf{x}_R^l$  and previous BiDIAF  $\mathbf{x}_A^l$  (if exists) unit along with an input image  $\mathbf{I}$  as an input and produces two outputs that are given as input to the next RCU  $\mathbf{x}_M^{l+1}$  and next BiDIAF block  $\mathbf{x}_A^{l+1}$ . We can formulate BiDIAF unit as:

$$\mathbf{x}_A^{l+1} = \mathcal{F}_B([\mathbf{x}_R^l, \mathcal{F}_I(\mathbf{I}), \mathcal{F}_P(\mathbf{x}_A^l)]) \quad (1)$$

$$\mathbf{x}_M^{l+1} = \mathbf{x}_R^l + \mathbf{x}_A^{l+1} \quad (2)$$

The function  $\mathcal{F}_P$  projects  $\mathbf{x}_A^l$  to the same dimensionality as  $\mathbf{x}_R^l$  using  $1 \times 1$  convolution. The function  $\mathcal{F}_I$  first sub-samples  $\mathbf{I}$  to the same spatial dimensions as  $\mathbf{x}_R^l$  using  $3 \times 3$  average pooling operation and then projects the sub-sampled image to the same dimensionality as  $\mathbf{x}_R^l$  using  $5 \times 5$  convolution. Apart from projection,  $5 \times 5$  convolution also learns input relevant feature maps. The function  $\mathcal{F}_B$  concatenates the feature maps obtained from  $\mathbf{x}_R^l$ ,  $\mathcal{F}_I(\mathbf{I})$ , and  $\mathcal{F}_P(\mathbf{x}_A^l)$ , followed by  $1 \times 1$  convolution that projects the concatenated feature maps to the same dimensionality as  $\mathbf{x}_R^l$ .

CNNs for classification does not encode the localization information explicitly. Existing methods use labeled data to learn the localization mask. For example, [22], [23] follows a bottom-up pyramid-based approach for learning the localization mask. Data labeling is an expensive task and therefore, we propose a two-fold strategy to generate localization mask: (1) aggregate the feature maps at different spatial-levels to create a candidate mask, and (2) refine the localization masks by jointly training a classification and localization network, assuming candidate masks as ground truth during training.

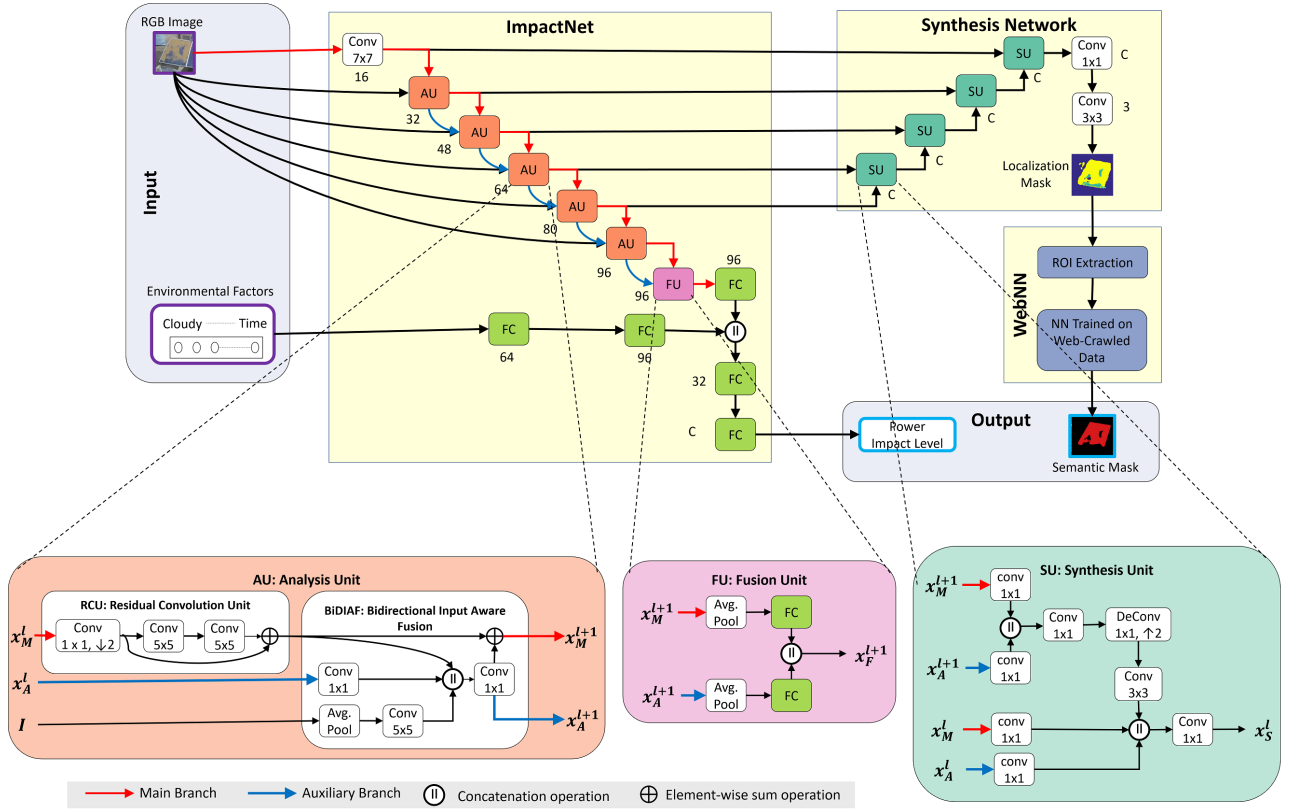


Fig. 4: DeepSolarEye: An end-to-end system for predicting the soiling impact, the soiling localization, and the soiling type simultaneously. Number of feature maps used by each block are reported next to it. Best viewed in color.

### B. Parameter-free Candidate Mask Creation

Our approach for localizing the region of impact is motivated by Burt and Adelson’s Laplacian Pyramid-based method [24], which encode and decode the image information using top-down (analysis) and bottom-up (synthesis) pyramids respectively. Standard CNNs aggregate feature maps in top-down fashion; thus suggesting their resemblance with the analysis network. Therefore, we can decode the encoded feature maps using a synthesis pyramid i.e. in bottom-up fashion for localizing the impact area. Figure 5 visualizes the pyramid-based approach for candidate mask creation.

Our synthesis pyramid fuses the feature maps of main  $x_M^l$  and auxiliary  $x_A^l$  branch at level  $l$  using Eq. 3 to produce a localization mask  $x_{mask}^l$ , which is then up-sampled to the same size as level  $l - 1$  using a bilinear interpolation. This process is repeated till the size of localization mask is the same as an input image  $I$ .

$$x_{mask}^l = (x_M^l \otimes x_A^l) \oplus x_A^l \quad (3)$$

where  $\otimes$  and  $\oplus$  are element-wise multiplication and additive operations. The element-wise multiplication operation helps in filtering the low-frequency components while element-wise addition helps in boosting the high-frequency components; thereby helping in efficiently localizing the impact area. Our causal inspection of feature maps at different spatial levels reveals that  $x_A^l$  has much more descriptive power than  $x_M^l$ , and therefore, we boost the high-frequency components using  $x_A^l$  (see Figure 6).

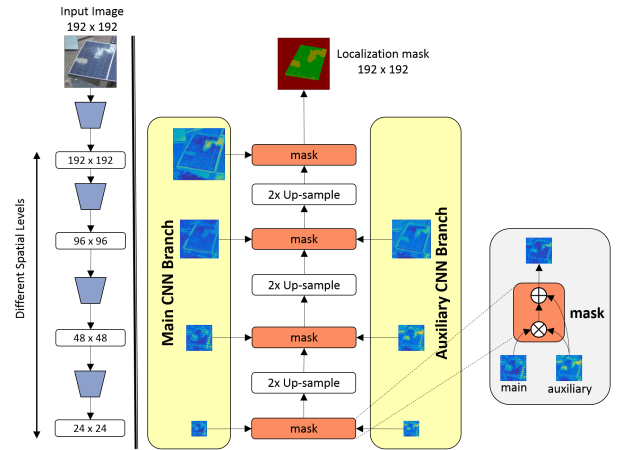


Fig. 5: Pyramid-based approach for candidate mask creation.

**Mask to label image:** Solar panel image can be split into three classes: background, solar panel, and soiling area. We detect the solar panel by performing Gaussian filtering and edge detection operations on an RGB image. The area outside detected solar panel is assigned a label of 1 (corresponding to background). The area within the detected panel is then thresholded using the mean of the mask. If the pixel value (inside panel) in the mask is less than the mean, then it is assigned a label of 2 (corresponding to panel). Otherwise, we

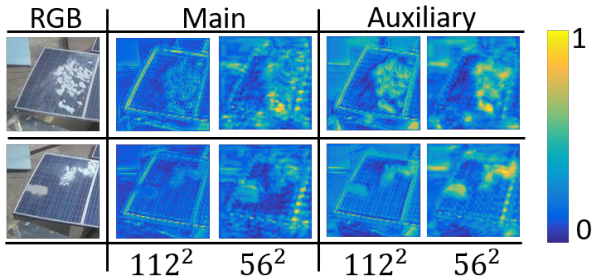


Fig. 6: Visualization of feature maps in main and auxiliary branches in the ImpactNet network. For visualization, we have scaled the feature maps to the same scale. Best viewed in color.

assign a label of 3 (corresponding to soiling area).

### C. Mask FCNN

Mask FCNN is a fully convolutional CNN that aims to simultaneously predict the soiling impact and the soiling area (localization). Our approach is motivated by the recently proposed method, Mask R-CNN [7], that applies classification and masking in *parallel*. Unlike Mask R-CNN that adopts two stage procedure (region proposal network followed by classification and masking network), our method is fully convolutional i.e. we do not use any region proposal network.

Mask FCNN is composed of two networks: 1) the classification network, the ImpactNet, and 2) synthesis network as shown in Figure 4. For synthesis network, we follow the fully convolutional bottom-up approach (e.g. [18], [25], [20]). Bottom-up approaches up-sample the feature maps to invert the loss of information due to down-sampling operations. Our bottom-up architecture is a stack of synthesis units (SU) (Figure 4), which can be mathematically defined as:

$$\mathbf{x}_S^l = \mathcal{F}_D(\{\mathbf{x}_M^l, \mathbf{x}_A^l, \mathbf{x}_M^{l+1}, \mathbf{x}_A^{l+1}\}) \quad (4)$$

$\mathcal{F}_D$  is a composite function comprising of  $1 \times 1$  convolution,  $1 \times 1$  deconvolution, and  $3 \times 3$  convolution operations.  $1 \times 1$  convolution operation reduce the dimension of the feature maps of  $\mathbf{x}_M^l$  and  $\mathbf{x}_A^l$  to  $C$ -dimensional space while  $1 \times 1$  deconvolution up-samples the feature maps of  $\mathbf{x}_M^{l+1}$  and  $\mathbf{x}_A^{l+1}$  to the same spatial dimensions as  $\mathbf{x}_M^l$  and  $\mathbf{x}_A^l$  along with projecting the feature maps to  $C$ -dimensional space. Mask FCNN was trained by minimizing the multi-task loss  $L_{multi} = L_{cls} + L_{mask}$ , where  $L_{cls}$  and  $L_{mask}$  are multinomial cross-entropy loss functions for classification (soiling impact) and masking (soiling area) respectively.

Cleaning actions for solar panels are dependent upon soiling type. For example, potential cleaning actions for bird drop and dust are wiping and air blow respectively. Therefore, it becomes critical to determine the soiling type for efficiently managing the work-force at solar farms. To determine the soiling type, we use a webly supervised classification network (WebNN).

### D. WebNN: Webly Supervised Neural Network

Given an image of solar panel with soiling mask, WebNN determines the soiling type. WebNN utilizes large amount of web data to train a soiling type classifier inspired from [26]. First, we collected images from the Internet by querying most common soiling categories including the ones which are not available in our dataset. 24-dimensional RGB histogram of each of these images were extracted as feature vectors. A small 3-layered neural network, with 50, 100, and 150 hidden neurons per layer respectively, was trained on these feature vectors to predict the soiling type.

To assign a label to the soiling area, we crop the RGB area (referred as ROI in Figure 4) corresponding to the soiling area in the localization mask. A 24-dimensional RGB histogram is then computed for this ROI as a feature vector which is then classified using WebNN to predict the soiling type.

## V. EXPERIMENTS AND RESULTS

We performed thorough experiments with various training and model choices on the PV-Net data. We compared classification and localization accuracies of our model, DeepSolarEye. We found that the proposed BiDIAF block improves the classification and localization capabilities of ResNet. We tested the generalizability of our method on images downloaded from the Internet and found that our method was extensible to incorporate the soiling types that were not present in our dataset.

### A. Classification Models and Results

**Models:** We trained and tested 3 different classification models with single input and single output (SISO) setting (Panel image as input and power loss level as output). Our proposed method (ImpactNet) was compared with its two alternatives. For the first alternative (referred as ImpactNet-A), the BiDIAF block was removed. The resultant network after removing BiDIAF block is the same as ResNet [14]. For the second alternative (referred as ImpactNet-B), we modified the BiDIAF Eq. 2 from  $\mathbf{x}_M^{l+1} = \mathbf{x}_R^l + \mathbf{x}_A^{l+1}$  to  $\mathbf{x}_M^{l+1} = \mathbf{x}_R^l$  i.e. input-aware feature maps were not shared with the main branch.

Our model (ImpactNet) was trained and tested under multiple input and single output (MISO) setting (Panel image and environmental factors as inputs and power loss level as output). In our experiments, we used *solar irradiance* and timestamp at which image was taken as environmental factors. To fuse these multiple inputs, we tried two alternatives: element-wise sum (ImpactNet-C) and concatenation (ImpactNet-D). Solar irradiance was an important factor as it captures environmental conditions (such as cloudy and sunny) indirectly, which influences the power loss [27].

**Training:** We trained all of our models end-to-end for 90 epochs using SGD with an initial learning rate of 0.01 decaying it by a factor of 10 after every 30 epochs, momentum of 0.9, weight decay of 0.0005, and a batch size of 32 on a single NVIDIA TitanX GPU. We used spatial dropout [28] with a dropout probability of 0.2 after every analysis unit (Figure 4).

The PV-Net dataset (N=45,754) was split randomly into training (N=27,537) and validation (N=18,217) sets. We binned the normalized power loss into  $C$  equal bins, with

each bin representing a soiling impact level (or class). In our experiments, we varied  $C$  from 2 to 16. Inverse class probability weighting scheme was used in loss function to address the class-imbalance issue.

Further, we augmented our data using standard augmentation techniques such as horizontal flips, vertical flips, and random rotations. We did not use any color-based augmentation strategies because the color and power generation capacity of the solar panel are directly influenced by the environmental factors, such as sunlight.

**Weight initialization:** We trained ResNet-18 on a subset of our dataset (training and validation sets each having 2,000 images) for 4-class classification task, with two different initialization strategies: (1) random weight initialization [29], and (2) fine-tuning the model that was trained on the ImageNet. Both networks attained similar accuracy for the 4-class classification task ( $95\% \pm 1\%$ ). Our casual inspection of feature maps revealed that the network initialized with random weights paid attention to the dataset-specific features (Figure 7). Therefore, we initialized the network weights randomly.

**Results:** Removing the BiDIAF unit in the ImpactNet network reduces the accuracy by about 2% (for both 8-class and 16-class network). Further, when we modified the BiDIAF unit to share the input-aware feature maps with the auxiliary CNN branch only, then the accuracy of the network is reduced by about 1%. The increase in classification accuracy with BiDIAF block is likely due to the fact that it promotes learning of data-specific features even at low-spatial resolutions (see Figure 8).

By adding environmental factors as input, the accuracy improved by about 2%. The improvement in the accuracy is not drastic; suggesting that ImpactNet is able to learn the complex behavior between environmental factors and soiling that leads to power loss.

To check the performance of our best method (ImpactNet-D) in real-world, we collected data from our experimental setup for additional 3 weeks. For 8-classes, ImpactNet-D was able to attain an accuracy of 84.5.%

### B. Localization Results

**Model and training details:** For localization experiments, we first computed the candidate masks using pyramid-based

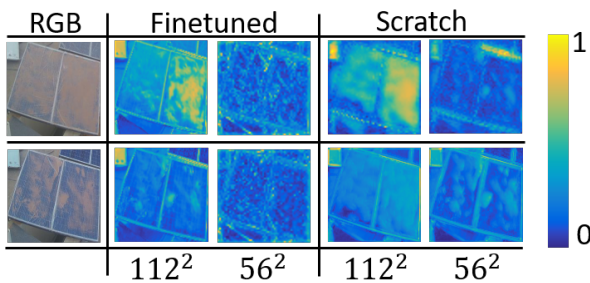


Fig. 7: Visualization of feature maps at different spatial resolutions with two different weight initialization strategies. Random weight initialization helped in learning dataset-specific feature maps. For visualization, we scaled the feature maps to the same scale. Best viewed in color.

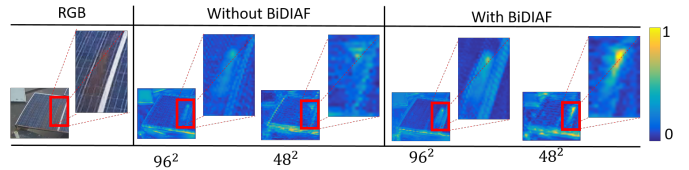


Fig. 8: Visualization of feature maps with and without BiDIAF. BiDIAF promotes data-specific feature learning, even at low spatial resolutions. Best viewed in color.

	Models	Classes				# Params (in Million)
		2	4	8	16	
SISO	ImpactNet	97.56	<b>93.39</b>	82.02	68.43	1.97
	ImpactNet-A	97.77	93.24	80.03	66.68	1.96
	ImpactNet-B	97.61	93.18	80.99	67.88	1.97
MISO	ImpactNet-C	97.64	93.10	82.97	70.19	1.99
	ImpactNet-D	<b>97.82</b>	93.28	<b>83.32</b>	<b>70.59</b>	1.99

TABLE I: This table compares top-1 accuracies of different models on our dataset. Note that ImpactNet-A is the same as ResNet [14].

method, which were then refined using Mask FCNN. We used the same training and augmentation strategy, as discussed in above section. Note that Mask FCNN learned about 2.12 million parameters.

**Evaluation metrics:** We evaluated the localization performance of our method both subjectively and objectively. For subjective assessment, we computed a *mean opinion score (MOS)*, while for objective assessment, we measured *Jaccard Index (JI)*, a widely used metric for measuring the localization accuracy.

For measuring the MOS, we randomly selected images from our dataset at an interval of 10 minutes; resulting in 579 images. For each image, we asked following four questions to the user to determine the localization accuracy:

- Q1:** How many regions of dust that were present in RGB image, but not in the localization mask?
- Q2:** How many regions of dust that were detected in localization mask, but not present in the RGB image?
- Q3:** On a scale of 0 to 10, rate the level of under-segmentation with 0 being perfectly segmented and 10 being fully under-segmented.
- Q4:** On a scale of 0 to 10, rate the level of over-segmentation with 0 being perfectly segmented and 10 being fully over-segmented.

If the area detected in a localization mask was half (or double) of the region of dust in an RGB image, then it was fully under-segmented (or over-segmented).

For measuring the JI, we selected a subset of 241 images out of 579 images. This subset includes all images where we noted high variance in the subjective assessment. These images are then annotated by the humans using LabelMe annotation tool [30]. We asked human annotators to annotate the dust regions on the solar panel image along with the dust type (such

Method		JI (in %)
Pyramid-based	w/o BiDIAF	38
	w/ BiDIAF	42
Mask FCNN		66

TABLE II: Objective assessment results

as brown and gray). These images were used as a ground truth for measuring the localization accuracy (JI).

**Subjective assessment results:** For sufficient cultural, gender, and racial diversity, we used Amazon Mechanical Turk for conducting this experiment. A total of 172 unique users participated in our study, with each image rated by 5 different users. MOS is shown in Figure 9.

- (i) Across all questions, overall MOS was lower than MOS for soiled (or dusty) panels; suggesting most of the mistakes were made on the soiled panels. However, MOS for soiled images is very less. On soiled images, our method was not able to locate about 2 soiled patches (Q1) while falsely detecting about 0.5 soiled patches (Q2) per image.
- (ii) The MOS for under-segmented (Q3) and over-segmented (Q4) images were almost the same and close to 0 (on a scale of 0 to 10). This suggests that the over- and under-segmentation results were not severe.

**Objective assessment results:** Table II compares the performance of three methods. First two methods used pyramid-based approach for generating the candidate masks while the third method was our end-to-end method, Mask FCNN. For a fair comparison between these models, we masked the background area (non-panel area) and did not consider it while measuring JI. From Table II, we can see that BiDIAF unit increases the JI of ResNet (or ImpactNet-A) by about 4%. This indicates that it helped in learning input-specific features which resulted in good localization capabilities. Further, Mask FCNN improves the JI of pyramid-based method (with BiDIAF) by about 24%; suggesting joint learning enables efficient aggregation of feature maps from the classification network.

**Webly supervised labeling results:** For measuring the labeling accuracy of WebNN, we used the same 241 images that were annotated by the human along with the type of dust. With webly supervised labeling, we achieved a classification accuracy of about 96.24%.

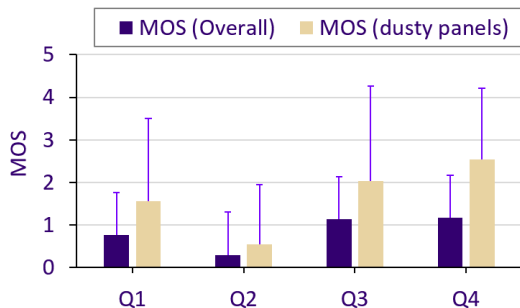


Fig. 9: Subjective assessment results. Best viewed in color.

To test the flexibility of WebNN in the Wild, we queried the Internet for solar panel images with a keyword (e.g. solar panel image with snow) and downloaded 150 such images. The images with low quality (either they were overlaid with text or image resolution was less than  $100 \times 100$ ) were manually discarded. After discarding such images, we were left with 50 images. Out of these 50 images, some of the images had multiple panels and were manually cropped to identify the panel area corresponding to the given keyword. These images were then fed into Mask FCNN to produce the localization mask, which were then classified using WebNN. Our method attained an accuracy of about 87% on these web images. Note that DeepSolarEye was able to localize the impact area (using Mask FCNN) and identify soiling type (using WebNN) even on the images and soiling types (e.g. snow, crack, and bird drop) that were not present in our dataset (see Figure 1); suggesting that DeepSolarEye had good generalization properties.

## VI. APPLICATION IN SOLAR FARM MAINTENANCE

*DeepSolarEye* provides an enriched information about solar panel soiling and defects (soiling impact, soiling localization, and soiling type). Further, soiling localization could be used to easily compute soiling coverage area. Such information could be used for efficient solar farm monitoring and maintenance. Work force management is one of the crucial task in solar farm management, especially when the farm is spread across several acres. Managing such farm requires to address two main questions: 1) How to clean? and 2) When to clean?.

The first question can be answered using the soiling type while the second question can be answered using soiling impact and soiling coverage area (computed from the soiling localization mask). To achieve this, we build a simple decision tree based on the soiling impact, soiling localization, and soiling type. Some results of this decision tree can be seen in Figure 1. In Figure 1(c), DeepSolarEye correctly identified soiling type (dust) and suggested correct cleaning type (air blow). Though the soiling impact is low (12.5% to 25%) the soiling coverage is about 30% of the actual panel area. Therefore, the suggested action along with the priority is *high*. The low impact level is primarily due to the environmental factors (cloudy day). For more results, see the supplementary material.

## VII. CONCLUDING REMARKS

In this paper, we presented a first deep learning based application for solar PV image analysis. We proposed a novel fully convolutional neural network based approach which takes an RGB image of solar panel and environmental factors (optional) as inputs to predict power loss, soiling localization, and soiling category. We proposed a four-stage methodology to train DeepSolarEye in weakly supervised fashion and completely avoids human labeled localization data. We introduced a novel BiDIAF block for superior localization capabilities. We, further, leverage the web-crawled data for categorizing the soiling type, which allows inclusion of new soiling types without re-training the Mask FCNN. Our empirical study suggests that BiDIAF module improves the classification and localization capabilities of ResNet by about 3% and 4%. Our end-to-end model yields further improvement of about 24% on localization task when learned in a weakly supervised manner.

Additionally, we introduced first of its kind dataset for solar panel image analysis consisting 45,000+ images.

To study the generalization of our model in different domains, we experimented with publicly available plant disease dataset [31]. We found that BiDIAF improved the localization capabilities of ResNet while achieving state-of-the-art classification accuracy of about 97% (see Appendix B for details).

## REFERENCES

- [1] Solar Energy Industries Association(USA), "Solar Market Insight," <http://www.seia.org/research-resources/solar-market-insight-2015-q4>, 2015.
- [2] T. Sarver, A. Al-Qaraghuli, and L. L. Kazmerski, "A comprehensive review of the impact of dust on the use of solar energy: History, investigations, results, literature, and mitigation approaches," *Renewable and Sustainable Energy Reviews*, vol. 22, pp. 698 – 733, 2013.
- [3] M. Mani and R. Pillai, "Impact of dust on solar photovoltaic (pv) performance: Research status, challenges and recommendations," *Renewable and Sustainable Energy Reviews*, vol. 14, no. 9, pp. 3124 – 3131, 2010.
- [4] M. R. Maghami, H. Hizam, C. Gomes, M. A. Radzi, M. I. Rezadad, and S. Hajjghorbani, "Power loss due to soiling on solar panel: A review," *Renewable and Sustainable Energy Reviews*, vol. 59, pp. 1307 – 1316, 2016.
- [5] J. W. Zapata, M. A. Perez, S. Kouro, A. Lensu, and A. Suuronen, "Design of a cleaning program for a pv plant based on analysis of energy losses," *IEEE Journal of Photovoltaics*, vol. 5, no. 6, pp. 1748–1756, Nov 2015.
- [6] S. Ren, K. He, R. Girshick, and J. Sun, "Faster r-cnn: Towards real-time object detection with region proposal networks," in *Advances in neural information processing systems*, 2015, pp. 91–99.
- [7] K. He, G. Gkioxari, P. Dollár, and R. Girshick, "Mask R-CNN," *IEEE International Conference on Computer Vision*, 2017.
- [8] M. Aghaei, A. Gandelli, F. Grimaccia, S. Leva, and R. Zich, "IR real-time analyses for PV system monitoring by digital image processing techniques," in *IEEE Conference on Event-based Control, Communication, and Signal Processing (EBCSCP)*. IEEE, 2015, pp. 1–6.
- [9] W. K. Yap, R. Galet, and K. C. Yeo, "Quantitative analysis of dust and soiling on solar pv panels in the tropics utilizing image-processing methods," in *Asia Pacific Solar Research Conference 2015*. Australian PV Institute, 2015.
- [10] S. Dotenco, M. Dalsass, L. Winkler, T. Würzner, C. Brabec, A. Maier, and F. Gallwitz, "Automatic detection and analysis of photovoltaic modules in aerial infrared imagery," in *IEEE Winter Conference on Applications of Computer Vision (WACV)*. IEEE, 2016, pp. 1–9.
- [11] M. Aghaei, S. Leva, and F. Grimaccia, "PV power plant inspection by image mosaicing techniques for IR real-time images," in *43rd IEEE Photovoltaic Specialists Conference (PVSC)*, June 2016, pp. 3100–3105.
- [12] K. Simonyan and A. Zisserman, "Very deep convolutional networks for large-scale image recognition," *arXiv preprint arXiv:1409.1556*, 2014.
- [13] C. Szegedy, W. Liu, Y. Jia, P. Sermanet, S. Reed, D. Anguelov, D. Erhan, V. Vanhoucke, and A. Rabinovich, "Going deeper with convolutions," in *Proceedings of the IEEE conference on computer vision and pattern recognition*, 2015, pp. 1–9.
- [14] K. He, X. Zhang, S. Ren, and J. Sun, "Deep residual learning for image recognition," in *The IEEE Conference on Computer Vision and Pattern Recognition (CVPR)*, June 2016.
- [15] G. Huang, Z. Liu, L. van der Maaten, and K. Q. Weinberger, "Densely connected convolutional networks," in *Proceedings of the IEEE Conference on Computer Vision and Pattern Recognition*, 2017.
- [16] L.-C. Chen, G. Papandreou, I. Kokkinos, K. Murphy, and A. L. Yuille, "Deepplab: Semantic image segmentation with deep convolutional nets, atrous convolution, and fully connected crfs," *arXiv preprint arXiv:1606.00915*, 2016.
- [17] R. Girshick, J. Donahue, T. Darrell, and J. Malik, "Rich feature hierarchies for accurate object detection and semantic segmentation," in *IEEE conference on computer vision and pattern recognition*, 2014, pp. 580–587.
- [18] V. Badrinarayanan, A. Kendall, and R. Cipolla, "Segnet: A deep convolutional encoder-decoder architecture for scene segmentation," *IEEE transactions on pattern analysis and machine intelligence*, 2017.
- [19] E. Shelhamer, J. Long, and T. Darrell, "Fully convolutional networks for semantic segmentation," *IEEE transactions on pattern analysis and machine intelligence*, vol. 39, no. 4, pp. 640–651, 2017.
- [20] O. Ronneberger, P. Fischer, and T. Brox, "U-net: Convolutional networks for biomedical image segmentation," in *International Conference on Medical Image Computing and Computer-Assisted Intervention*. Springer, 2015, pp. 234–241.
- [21] G. Lin, A. Milan, C. Shen, and I. Reid, "Refinenet: Multi-path refinement networks with identity mappings for high-resolution semantic segmentation," *CVPR*, 2017.
- [22] B. Hariharan, P. Arbeláez, R. Girshick, and J. Malik, "Hypercolumns for object segmentation and fine-grained localization," in *Proceedings of the IEEE Conference on Computer Vision and Pattern Recognition*, 2015, pp. 447–456.
- [23] G. Ghiasi and C. C. Fowlkes, "Laplacian pyramid reconstruction and refinement for semantic segmentation," in *European Conference on Computer Vision*. Springer, 2016, pp. 519–534.
- [24] P. Burt and E. Adelson, "The laplacian pyramid as a compact image code," *IEEE Transactions on communications*, vol. 31, no. 4, pp. 532–540, 1983.
- [25] H. Noh, S. Hong, and B. Han, "Learning deconvolution network for semantic segmentation," in *Proceedings of the IEEE International Conference on Computer Vision*, 2015, pp. 1520–1528.
- [26] X. Chen and A. Gupta, "Webly supervised learning of convolutional networks," in *Proceedings of the IEEE International Conference on Computer Vision*, 2015, pp. 1431–1439.
- [27] B. Andò, S. Baglio, A. Pistorio, G. M. Tina, and C. Ventura, "Sentinella: Smart monitoring of photovoltaic systems at panel level," *IEEE Transactions on Instrumentation and Measurement*, vol. 64, no. 8, pp. 2188–2199, 2015.
- [28] J. Tompson, R. Goroshin, A. Jain, Y. LeCun, and C. Bregler, "Efficient object localization using convolutional networks," in *Proceedings of the IEEE Conference on Computer Vision and Pattern Recognition*, 2015, pp. 648–656.
- [29] K. He, X. Zhang, S. Ren, and J. Sun, "Delving deep into rectifiers: Surpassing human-level performance on imagenet classification," in *Proceedings of the IEEE international conference on computer vision*, 2015, pp. 1026–1034.
- [30] B. C. Russell, A. Torralba, K. P. Murphy, and W. T. Freeman, "Labelme: A database and web-based tool for image annotation," *International Journal of Computer Vision*, vol. 77, no. 1, pp. 157–173, May 2008.
- [31] S. Sladojevic, M. Arsenovic, A. Anderla, D. Culibrk, and D. Stefanovic, "Deep neural networks based recognition of plant diseases by leaf image classification," *Computational intelligence and neuroscience*, vol. 2016, 2016.



## APPENDIX

### A. Classification Error Analysis

Figure 10a visualizes the confusion matrix for 8-class case. We can see that the majority of the mistakes are made with the neighboring classes. Since we binned the classes at fixed interval, it becomes critical to understand the mistakes made by our network i.e. mistakes are made near the boundary or towards the extreme end of the neighboring classes. We introduced a relaxing variable  $\alpha$  that relaxes the boundaries of each impact level bin. For example, if the range of the bin is between 12.5% to 25%, then after relaxation, the range will be  $12.5\% - \alpha$  to  $25\% + \alpha$ . Figure 10b shows a graph between  $\alpha$  and accuracy. When we increased  $\alpha$  from 0 to 0.01, the accuracy of our method increased from about 83% to about 88%; suggesting the mistakes are at the border of the bin and are tolerable.

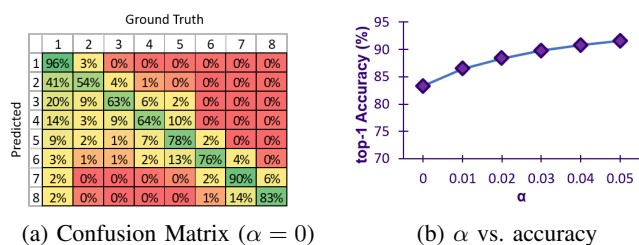


Fig. 10: Impact on accuracy after boundary conditions are relaxed by a threshold  $\alpha$ . Best viewed in color.

### B. Experiments with Plant Disease Dataset

Towards the generalization of our model in other domain for localization task, we experimented with the publicly available plant disease dataset. We trained and tested our model, ImpactNet, with and without BiDIAF for plant disease classification task. In both cases, our model attained an accuracy of around 97%, which is comparable to the method proposed by [31]. However, on casual visual inspection, we found that ImpactNet without BiDIAF pays more attention to leaf area (such as medrib and veins) while with BiDIAF, it pays more attention to disease area (Figure 12). This suggests that BiDIAF has promising localization capabilities in other domains.

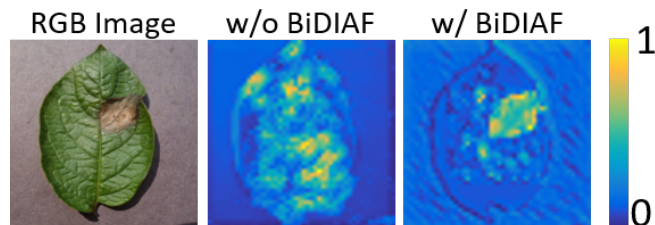


Fig. 11: Feature map visualization with and without BiDIAF. Best viewed in color.

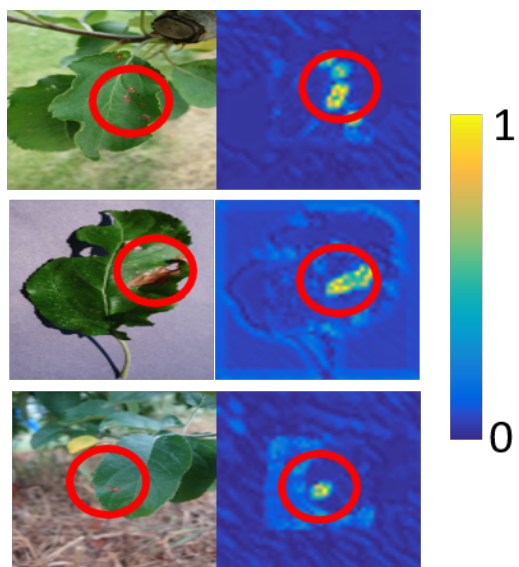


Fig. 12: More feature map visualizations with BiDIAF unit on the plant disease dataset. Red circles denote the disease area. Best viewed in color.

### C. Soiling Results

Figures 13 and 14 depict the performance of our method on different solar panel images (either from our dataset or downloaded from the Internet). We can see that the proposed method has good localization and soiling classification properties.

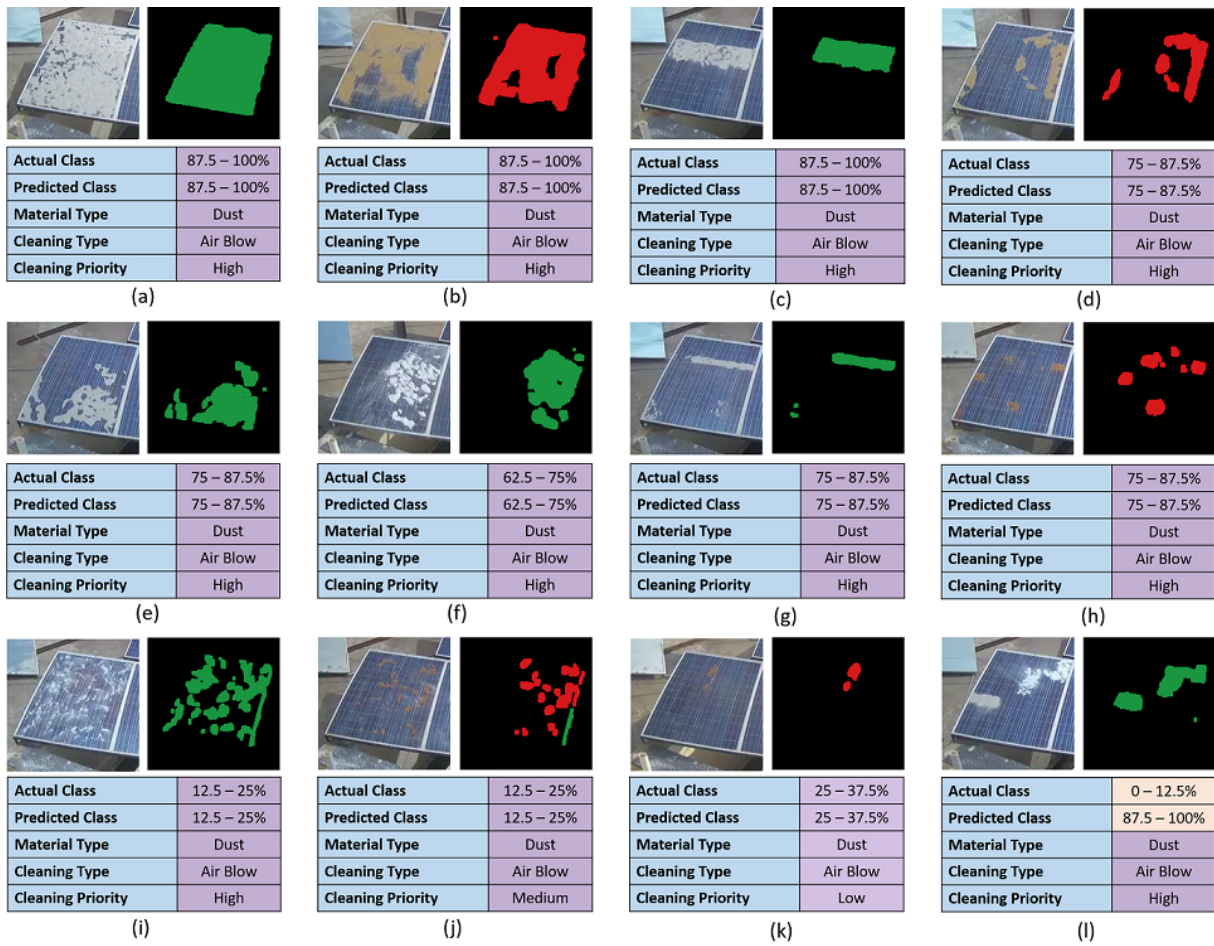


Fig. 13: Images (from our dataset) depicting the performance of our method. Best viewed in color.

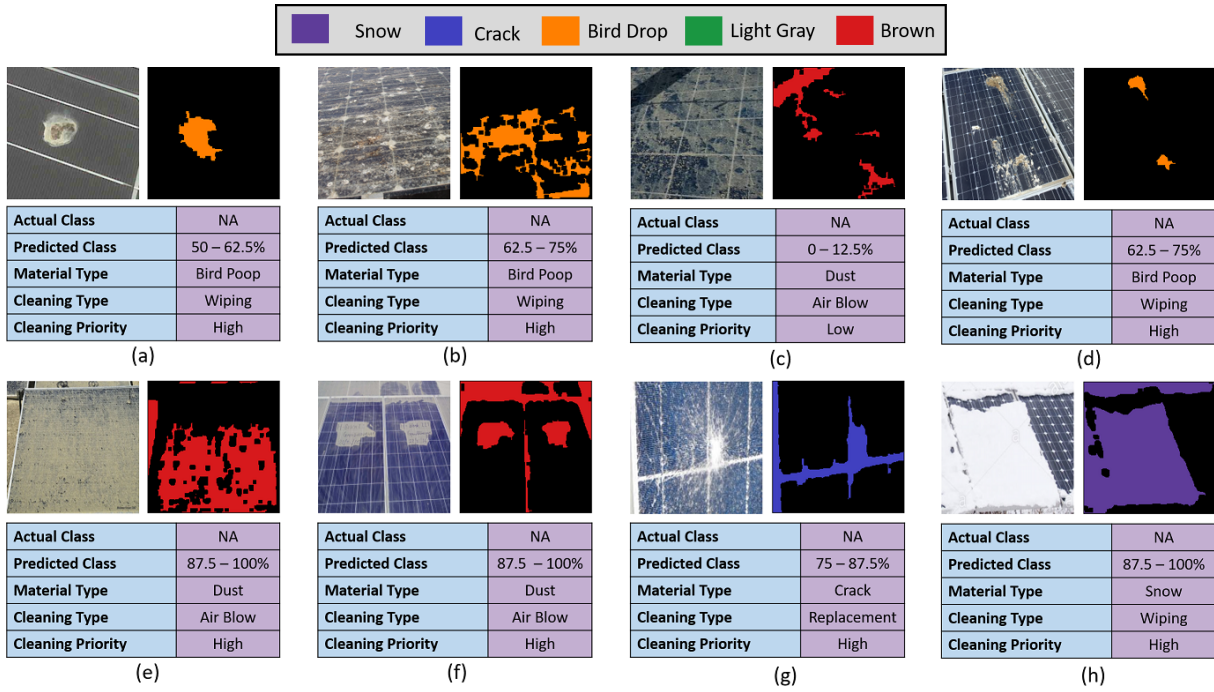


Fig. 14: Images (from the Internet) depicting the performance of our method. Best viewed in color.